



ODTÜ METU

**ME485: Computational Fluid Dynamics
Using Finite Volume Method**

Homework 4

Uğur Ozan Baygeldi

Ali Kaya

Onur Kakilli

Group 15

1 Introduction

This homework is different from the first three as there is no need to implement any code. (Baygeldi-Kaya-Kakilli 2025) Instead, this homework requires an analysis of the methods implemented to $me_{\nu}m$, asking for a comparison of the different convection flux computation methods implemented under different initial conditions, boundary conditions, and using different time discretization methods.

2 Roadmap

As there is no need to implement any code, there is no `system.py` to give guidance. Thankfully, the homework document provides sufficient direction. (Karakuş 2024) The report will cover the following, with text in brackets indicating the implemented name within $me_{\nu}m$:

- Explanation of the Convection Flux Computation Methods
 - Roe [`roe`]
 - RoeM [`roem`]
 - Rotated-RoeM [`rotated-roem`]
 - AUSMPW+ [`ausmpw+`]
 - AUSM⁺-up [`ausm+up`]
 - HLLEM [`hllem`]
 - Rusanov [`rusanov`]
- Explanation of the Benchmark Problems
 - Double Mach Reflection (Canceled)
 - Forward Facing Step
 - Flow Over a Circular Bump

- Scramjet Inlet Flow Model with Different Boundary Conditions [`slip-wall`, `sup-in`, `sub-outp`, `far`]

Essentially this report covers a variety of topics commonly encountered in the CFD world.

3 Explanation of the Convection Flux Computation Methods

In this chapter, the convective flux computation methods utilized in this report will be summarized.

3.1 Roe [`roe`]

Roe method attempts to find a Jacobian matrix $A = \partial \mathbf{F} / \partial \mathbf{u}$ such that:

$$\begin{aligned} \mathbf{u}_t + \mathbf{F}_x &= 0 \\ \mathbf{u}(x, 0) &= \mathbf{u}_0(x) \end{aligned} \tag{1}$$

This A matrix is then approximated as \tilde{A} , a constant matrix, that satisfies the following conditions (Roe 1981):

- Constitutes a linear mapping from the vector space \mathbf{u} to the vector space \mathbf{F}
- As $\mathbf{u}_L \rightarrow \mathbf{u}_R \rightarrow \mathbf{u}$, $\tilde{A}(\mathbf{u}_L, \mathbf{u}_R) \rightarrow A(\mathbf{u})$
- $\forall \mathbf{u}_L, \mathbf{u}_R$, $\tilde{A}(\mathbf{u}_L, \mathbf{u}_R) \times (\mathbf{u}_L - \mathbf{u}_R) = \mathbf{F}_L - \mathbf{F}_R$
- Eigenvectors of \tilde{A} are linearly independent.

To meet the criteria, Roe follows the following path (Roe 1981):

$$\mathbf{u}(\theta) = \mathbf{u}_L + \theta(\mathbf{u}_R - \mathbf{u}_L), \quad d\mathbf{u} = (\mathbf{u}_R - \mathbf{u}_L)d\theta \tag{2}$$

$$\mathbf{F}(\mathbf{u}_R) - \mathbf{F}(\mathbf{u}_L) = \int_0^1 A(\theta)d\theta \cdot (\mathbf{u}_R - \mathbf{u}_L) \rightarrow \tilde{A} = \int_0^1 A(\theta)d\theta \tag{3}$$

Roe then moves to the Euler equations with \mathbf{w} being a parameter vector such that (Roe 1981):

$$\mathbf{u}_f + \mathbf{F}_x + \mathbf{G}_y + \mathbf{H}_z = 0 \quad (4)$$

$$\mathbf{w} = \rho^{1/2}(1, u, v, w, H)^T \quad (5)$$

Then the total energy is defined from the equation of state:

$$e = \frac{p}{(\gamma - 1)} + \frac{1}{2}\rho(u^2 + v^2 + w^2) \quad (6)$$

And total enthalpy is found using:

$$\rho H = e + p \quad (7)$$

Roe then simplifies the equations by normalizing them with \mathbf{w}_1 ($\rho^{1/2}$ term), for example:

$$u = \frac{\rho_L^{1/2}u_L + \rho_R^{1/2}u_R}{\rho_L^{1/2} + \rho_R^{1/2}} \quad (8)$$

Then the eigenvalues of the mapping (*Equation 4*) boils down to for $\Delta\mathbf{F} \rightarrow \Delta\mathbf{G}$:

$$(\lambda u - v)^3[(\lambda u - v)^2 - a^2(1 + \lambda^2)] = 0 \quad (9)$$

With the eigenvectors:

$$\mathbf{e}_1 = \begin{pmatrix} 1 \\ u + v/R \\ v - u/R \\ w \\ H \end{pmatrix}, \mathbf{e}_2 = \begin{pmatrix} 1 \\ 0 \\ 0 \\ 0 \\ -H \end{pmatrix}, \mathbf{e}_3 = \begin{pmatrix} w \\ 0 \\ 0 \\ 2H \\ wH \end{pmatrix}, \mathbf{e}_4 = \begin{pmatrix} 1 + \frac{1}{2}q^2/H \\ 2u \\ 2v \\ 2w \\ H + \frac{1}{2}q^2 \end{pmatrix}, \mathbf{e}_5 = \begin{pmatrix} 1 \\ u - v/R \\ v + u/R \\ w \\ H \end{pmatrix} \quad (10)$$

For the eigenvalues:

$$\lambda_1 = \frac{v - u/R}{u + v/R}, \lambda_2 = \frac{v}{u}, \lambda_3 = \frac{v}{u}, \lambda_4 = \frac{v}{u}, \lambda_5 = \frac{v + u/R}{u - v/R} \quad (11)$$

With:

$$R^2 = \frac{u^2 + v^2}{a^2} - 1 \quad (12)$$

Then:

$$\Delta \mathbf{F} = \sum_1^5 a_i \mathbf{e}_i \quad (13)$$

Which can be solved by the following set of equations:

$$\begin{aligned} 2Ha_2 &= H\Delta F_1 - \Delta F_5 \\ q^2 S &= u\Delta F_2 + v\Delta F_3 \\ 2Ha_3 &= \Delta F_4 - wS \\ (1 - \frac{1}{2}q^2/H)a_4 &= S + a_2 - \Delta F_1 \\ q^2(a_5 - a_1) &= R(u\Delta F_3 - v\Delta F_2) \\ a_5 + a_1 &= S - 2a_4 \end{aligned} \quad (14)$$

The code within *me_{f_v}m* seems to follow another implementation of the method though as the outputs are logical, the code works as intended.

3.2 RoeM [roem]

The *Roe scheme with Mach number-based function* scheme is a set of 2 equations named *RoeM 1* and *RoeM 2* derived from the Roe scheme for the following 3 cases (S.-s. Kim et al. 2003):

- Stationary contact discontinuity $\rightarrow u_c = 0, D^{(p)} = 0$
- Moving contact discontinuity with $T_j > T_{j+1} \rightarrow u_c \neq 0, \alpha = \hat{c}, \beta \neq \hat{c}, D^{(p)} = |u_c|$

- Moving contact discontinuity with $T_j < T_{j+1} \rightarrow u_c \neq 0, \alpha \neq \hat{c}, \beta = \hat{c}$,

$$D^{(p)} = \left| \frac{u_c}{(\alpha + \hat{c})(\hat{c} + u_c)} (3\hat{c}u_c + 3\alpha\hat{c} - \alpha u_c - \hat{c}^2) \right|$$

With,

$$b_1 = \max(0, \hat{U} + \hat{c}, U_{j+1} + \hat{c}), b_2 = \min(0, \hat{U} - \hat{c}, U_j - \hat{c}) \quad (15)$$

And the following:

$$\Delta \mathbf{Q}^* = \Delta \begin{pmatrix} \rho \\ \rho u \\ \rho v \\ \rho H \end{pmatrix}, \mathbf{B} \Delta \mathbf{Q} = \left(\Delta p - f \frac{\Delta p}{\hat{c}^2} \right) \begin{pmatrix} 1 \\ \hat{u} \\ \hat{b} \\ \hat{H} \end{pmatrix} + \hat{p} \begin{pmatrix} 0 \\ \Delta u - n_x \Delta U \\ \Delta v - n_y \Delta U \\ \Delta H \end{pmatrix} \quad (16)$$

RoeM 1 [Equation 17] and *RoeM 2* [Equation 18] is defined as the following (S.-s. Kim et al. 2003):

$$\mathbf{F}_{j+1/2} = \frac{b_1 \times \mathbf{F}_j - b_2 \times \mathbf{F}_{j+1}}{b_1 - b_2} + \frac{b_1 \times b_2}{b_1 - b_2} \Delta \mathbf{Q}^* - \frac{b_1 \times b_2}{b_1 - b_2} \times \frac{1}{1 + |\hat{M}|} \mathbf{B} \Delta \mathbf{Q} \quad (17)$$

$$\mathbf{F}_{j+1/2} = \frac{b_1 \times \mathbf{F}_j - b_2 \times \mathbf{F}_{j+1}}{b_1 - b_2} + \frac{b_1 \times b_2}{b_1 - b_2} \Delta \mathbf{Q}^* - g \frac{b_1 \times b_2}{b_1 - b_2} \times \frac{1}{1 + |\hat{M}|} \mathbf{B} \Delta \mathbf{Q} \quad (18)$$

The proposed schemes cover all the cases mentioned without an expansion shock. Due to the different implementation of Roe method, this method is also different from what is explained in the article for *me_fm* but again the results are as expected.

3.3 Rotated-RoeM [rotated-roem]

Similar to *RoeM*, the *Rotated-RoeM* scheme utilizes the same formulation explained in *section 3.2* with some changes. The first step is setting up the α angles (Choi et al. 2024):

$$\alpha_i = \mathbf{n}_i \cdot \mathbf{n}_f \quad (19)$$

$$\mathbf{n}_f = \alpha_1 \mathbf{n}_1 + \alpha_2 \mathbf{n}_2 \quad (20)$$

Where \mathbf{n}_1 is selected using the following, \mathbf{n}_2 is defined as the vector orthogonal to \mathbf{n}_1 :

$$\mathbf{n}_1 = \begin{cases} \mathbf{n}_f, & |\Delta \vec{V}| < \varepsilon \\ \mathbf{n}_v, & otherwise \end{cases} \quad (21)$$

$$\mathbf{n}_v = \frac{\Delta \vec{V}}{|\Delta \vec{V}|} \quad (22)$$

And with the following adjustments to *Equation 15*, and *Equation 16* and some additional definitions:

$$\tilde{b}_1 = \max(0, \hat{\tilde{U}} + \hat{c}, \tilde{U}_r + \hat{c}), \quad \tilde{b}_2 = \min(0, \hat{\tilde{U}} - \hat{c}, \tilde{U}_r - \hat{c}) \quad (23)$$

$$B\Delta\tilde{\mathbf{Q}} = \left(\Delta p - |\alpha_1| \frac{\Delta p}{\hat{c}^2} \right) \begin{pmatrix} 1 \\ \hat{u} \\ \hat{v} \\ \hat{H} \end{pmatrix} + \hat{\rho} \begin{pmatrix} 0 \\ \Delta u - n_{1,x} \Delta \tilde{U} \\ \Delta v - n_{1,y} \Delta \tilde{U} \\ \Delta H \end{pmatrix} \quad (24)$$

$$\hat{\tilde{U}} = (\hat{u}, \hat{v}) \cdot \mathbf{n}_1, \quad \hat{\tilde{M}} = \frac{\hat{\tilde{U}}}{\hat{c}} \quad (25)$$

The Rotated-RoeM flux is formulated as the following: (Choi et al. 2024):

$$\mathbf{H}^{R-RoeM}(\mathbf{Q}_L, \mathbf{Q}_R, \mathbf{n}_f) = \frac{b_1 \times \mathbf{F}_c(\mathbf{Q}_L) \cdot \mathbf{n}_f - b_2 \times \mathbf{F}_c(\mathbf{Q}_R) \cdot \mathbf{n}_f}{b_1 - b_2} + \frac{b_1 \times b_2}{b_1 - b_2} \Delta \mathbf{Q}^* - \alpha_1 \frac{\tilde{b}_1 \times \tilde{b}_2}{\tilde{b}_1 - \tilde{b}_2} \times \frac{1}{1 + |\hat{\tilde{M}}|} B\Delta\mathbf{Q} \quad (26)$$

3.4 AUSMPW+ [ausmpw+]

The *Advection Upstream Splitting Method by Pressure Based Weight Functions* (AUSMPW) is a method improving upon the already successful *Advection Upstream Splitting Method* (AUSM) which can accurately solve flows in a shear layer. (K. H. Kim, C. Kim, and Rho 2001) The AUSMPW method has beneficial features such as the elimination of overshoots, accurate numerical dissipation, preservation of total enthalpy, and elimination of the carbuncle phenomena (K. H. Kim, C. Kim, and Rho 2001) which are problems observed in the shape of the shockwave caused by the numerical methods employed. (Elling

2009)

Advection Upstream Splitting Method by Pressure Based Weight Functions + [ausmpw+] employs a new method for calculating the speed of sound numerically aiming to increase accuracy and efficiency. (K. H. Kim, C. Kim, and Rho 2001)

Essentially, the *AUSMPW+* method boils down to:

$$\mathbf{F}_{\frac{1}{2}} = \bar{M}_L^+ c_{\frac{1}{2}} \Phi_L + \bar{M}_R^- c_{\frac{1}{2}} \Phi_R + (P_L^+|_{\alpha=\frac{3}{16}} \mathbf{P}_L + P_R^- + |_{\alpha=\frac{3}{16}} \mathbf{P}_R) \quad (27)$$

Where the Mach numbers are dependent on the cell interface mach number ($m_{1/2}$):

if $m_{1/2} \geq 0$

$$\begin{aligned} \bar{M}_L^+ &= \bar{M}_L^+ + \bar{M}_R^- \cdot [(1-w)(1+f_R) - f_L] \\ \bar{M}_R^- &= \bar{M}_R^- \cdot w \cdot (1+f_R) \end{aligned} \quad (28)$$

if $m_{1/2} < 0$

$$\begin{aligned} \bar{M}_L^+ &= \bar{M}_L^+ \cdot w \cdot (1+f_L) \\ \bar{M}_R^- &= \bar{M}_R^- + \bar{M}_L^+ \cdot [(1-w)(1+f_L) + f_L - f_R] \end{aligned} \quad (29)$$

Where:

$$w(p_L, p_R) = 1 - \min\left(\frac{p_L}{p_R}, \frac{p_R}{p_L}\right)^3 \quad (30)$$

Lastly $f_{L,R}$ being:

$$f_{L,R} = \begin{cases} \left(\frac{p_{L,R}}{p_s} - 1\right) \min\left(1, \frac{\min(p_{1,L}, p_{1,R}, p_{2,L}, p_{2,R})}{\min(p_L, p_R)}\right)^2, & p_s \neq 0 \\ 0, & \text{otherwise} \end{cases} \quad (31)$$

With

$$p_s = P_L^+ p_L + P_R^- p_R \quad (32)$$

For better understanding, the following stencil may be used:

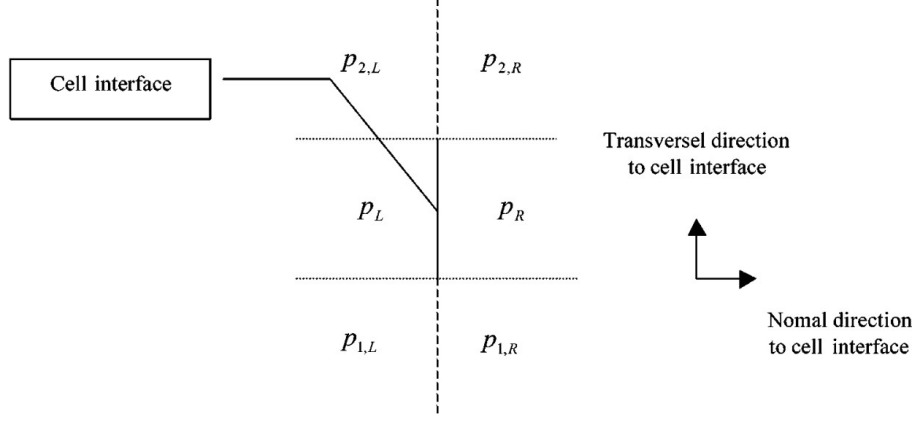


Figure 1: AUSMPW+ Stencil

The Mach number and pressure splitting functions used in the above equations are simplified to the following:

$$M^\pm = \begin{cases} \pm \frac{1}{4}(M \pm 1)^2, & |M| \leq 1 \\ \frac{1}{2}(M \pm |M|), & |M| > 1 \end{cases} \quad (33)$$

$$P^\pm|_\alpha = \begin{cases} \frac{1}{4}(M \pm 1)^2(2 \mp M) \pm \alpha M(M^2 - 1)^2, & |M| \leq 1 \\ \frac{1}{2}(1 \pm \text{sign}(M)), & |M| > 1 \end{cases} \quad (34)$$

With the speed of sound calculation done using the following:

$$\begin{aligned} \frac{1}{2}(U_L + U_R) > 0 : c_{\frac{1}{2}} &= \frac{c_s^2}{\max(|U_L|, c_s)} \\ \frac{1}{2}(U_L + U_R) < 0 : c_{\frac{1}{2}} &= \frac{c_s^2}{\max(|U_R|, c_s)} \end{aligned} \quad (35)$$

Using:

$$c_s = \sqrt{\frac{2(\gamma - 1)}{(\gamma + 1)H_{normal}}} \quad (36)$$

$$H_{normal} = 0.5(H_{total,L} - 0.5 \cdot V_L^2 + H_{total,R} - 0.5 \cdot V_R^2) \quad (37)$$

3.5 AUSM⁺-up [ausm+up]

Similar to the previous method, the *AUSM⁺up* method employs an *advection upstream splitting method* at its core, modifying it to achieve better robustness for low Mach

numbers aiming to maintain the convergence rate and accuracy while doing so. (Liou 2006) In the article, this task is completed by employing an asymptotic analysis under the limit of $M \rightarrow 0$. This method can be explained as follows:

First, define,

$$M_{L/R} = \frac{u_{L/R}}{a_{1/2}} \quad (38)$$

With $a_{1/2}$ being defined using the following set of equations:

$$a_{1/2} = \min(\hat{a}_L, \hat{a}_R) \quad (39)$$

$$\hat{a}_L = a^{*2} / \max(a^*, u_L) \quad (40)$$

$$\hat{a}_R = a^{*2} / \max(a^*, -u_R)$$

$$a^{*2} = \frac{2(\gamma - 1)}{\gamma + 1} H_t \quad (41)$$

Then the split Mach numbers with $\beta = \frac{1}{8}$:

$$\begin{aligned} \mathcal{M}_{(1)}^{\pm}(M) &= \frac{1}{2}(M \pm |M|) \\ \mathcal{M}_{(2)}^{\pm}(M) &= \pm \frac{1}{4}(M \pm 1)^2 \\ \mathcal{M}_{(4)}^{\pm}(M) &= \begin{cases} \mathcal{M}_{(1)}^{\pm}(M), & |M| \geq 1 \\ \mathcal{M}_{(2)}^{\pm}(M)(1 \mp 16\beta\mathcal{M}_{(2)}^{\mp}(M)), & \text{otherwise} \end{cases} \end{aligned} \quad (42)$$

The split pressure numbers can be defined using the split Mach numbers as the following with $\alpha = \frac{3}{16}$:

$$\mathcal{P}_{(5)}^{\pm}(M) = \begin{cases} \frac{1}{M}\mathcal{M}_{(1)}^{\pm}(M), & |M| \geq 1 \\ \mathcal{M}_{(2)}^{\pm}(M)[(\pm 2 - M) \mp 16\alpha M\mathcal{M}_{(2)}^{\mp}(M)], & \text{otherwise} \end{cases} \quad (43)$$

Furthermore, the following are defined:

$$\bar{M}^2 = \frac{(u_L^2 + u_R^2)}{2a_{1/2}^2} \quad (44)$$

$$M_o^2 = \min(1, \max(\bar{M}^2, M_\infty^2)) \quad (45)$$

$$f_a(M_o) = M_o(2 - M_o) \quad (46)$$

With $K_p = 0.25$ (which is set as 1 in the *meffvm* code) and $\sigma = 1$ the following equation yields the interface Mach number with $\rho_{1/2} = 0.5(\rho_L + \rho_R)$:

$$M_{1/2} = \mathcal{M}_{(4)}^+(M_L) + \mathcal{M}_{(4)}^-(M_R) - \frac{K_p}{f_a} \max(1 - \sigma \bar{M}^2, 0) \frac{p_R - p_L}{\rho_{1/2} a_{1/2}^2} \quad (47)$$

To define the pressure fluxes with $K_u = 0.75$ (which set as 1 in the *meffvm* code):

$$\dot{m}_{1/2} = a_{1/2} M_{1/2} \begin{cases} \rho_L, & M_{1/2} > 0 \\ \rho_R, & \text{otherwise} \end{cases} \quad (48)$$

$$p_{1/2} = \mathcal{P}_{(5)}^+(M_L) p_L + \mathcal{P}_{(5)}^-(M_R) p_R - K_u \mathcal{P}_{(5)}^+ \mathcal{P}_{(5)}^-(\rho_L + \rho_R) (f_a a_{1/2}) (u_R - u_L) \quad (49)$$

Lastly,

$$\mathbf{f}_{1/2} = \dot{m}_{1/2} \begin{cases} \vec{\psi}_L, & \dot{m}_{1/2} > 0 \\ \vec{\psi}_R, & \text{otherwise} \end{cases} + \mathbf{p}_{1/2} \quad (50)$$

Which mimics the flux function:

$$\mathbf{F} = \mathbf{F}^{(c)} + \mathbf{P} = \mathbf{f}_{1/2} \quad (51)$$

3.6 HLLEM [hllem]

The *Harten-Lax-van Leer-Einfeldt* (HLL) is a positively conservative scheme. The HLLEM scheme utilizes a modified Riemann solver. (Einfeldt et al. 1991)

Essentially the *modified HLL* scheme (HLLEM) according to the source is as follows

(Einfeldt et al. 1991):

$$\omega_{HLLLEM}(x'/t; i + 1/2) = \begin{cases} \mathbf{v}_i, & x' < b_{i+1/2}^l t \\ \mathbf{v}_{i+1/2} + (x - \bar{u}_{i+1/2} t) (\hat{\delta}_{i+1/2}^2 \hat{\alpha}_{i+1/2}^2 \hat{\mathbf{R}}_{i+1/2}^2 \\ \quad + \hat{\delta}_{i+1/2}^3 \hat{\alpha}_{i+1/2}^3 \hat{\mathbf{R}}_{i+1/2}^3), & b_{i+1/2}^l < x < b_{i+1/2}^r \\ \mathbf{v}_{i+1/2}, & b_{i+1/2}^r < x' \end{cases}, \quad (52)$$

Where $\hat{\mathbf{R}}_{i+1/2}^2$ and $\hat{\mathbf{R}}_{i+1/2}^3$ are the 2nd and 3rd eigenvectors of the Jacobian matrix $d\mathbf{f}(\hat{\mathbf{w}}_{i+1/2}) = A(\hat{\mathbf{w}}_{i+1/2})$. Where the required values for $\hat{\alpha}_{i+1/2}^2$, $\hat{\alpha}_{i+1/2}^3$ and $\bar{u}_{i+1/2}$ is found using:

$$\mathbf{v}_{i+1} - \mathbf{v}_i = \sum_{l=1}^4 \hat{\alpha}_{i+1/2}^l \hat{\mathbf{R}}_{i+1/2}^l \quad (53)$$

$$\bar{u}_{i+1/2} = \frac{b_{i+1/2}^r + b_{i+1/2}^l}{2} \quad (54)$$

The average state explained *here*, $\hat{\mathbf{w}}_{i+1/2} = (\hat{\rho}, \hat{u}, \hat{v}, \hat{c})^T$ is chosen as:

$$\hat{\rho}_{i+1/2} = \sqrt{\rho_i \rho_{i+1}} \quad (55)$$

$$\hat{u}_{i+1/2} = \frac{\sqrt{\rho_i} u_i + \sqrt{\rho_{i+1}} u_{i+1}}{\sqrt{\rho_i} + \sqrt{\rho_{i+1}}} \quad (56)$$

$$\hat{v}_{i+1/2} = \frac{\sqrt{\rho_i} v_i + \sqrt{\rho_{i+1}} v_{i+1}}{\sqrt{\rho_i} + \sqrt{\rho_{i+1}}} \quad (57)$$

$$\hat{H}_{i+1/2} = \frac{\sqrt{\rho_i} H_i + \sqrt{\rho_{i+1}} H_{i+1}}{\sqrt{\rho_i} + \sqrt{\rho_{i+1}}} \quad (58)$$

$$\hat{c}_{i+1/2}^2 = (\gamma - 1) \left[H_{i+1/2} - \frac{1}{2} (u_{i+1/2}^2 + v_{i+1/2}^2) \right] \quad (59)$$

The modified version defines the $\delta_{i+1/2}^2$ and $\delta_{i+1/2}^3$ as the following in order to take out excess dissipation (Einfeldt et al. 1991):

$$\delta_{i+1/2}^2 = \delta_{i+1/2}^3 = \frac{\hat{c}_{i+1/2}}{\hat{c}_{i+1/2} + |\bar{u}_{i+1/2}|} \quad (60)$$

With $b_{i+1/2}^l$ and $b_{i+1/2}^r$ being defined as the largest and the smallest eigenvalues of the

Roe-average matrix. (Einfeldt et al. 1991) The HLLEM scheme is written as:

$$\mathbf{f}_{i+1/2} = \frac{1}{2} \left[\mathbf{f}(\mathbf{v}_i) + \mathbf{f}(\mathbf{v}_{i+1}) - \sum_{R=1}^4 Q_{i+1/2}^R \alpha_{i+1/2}^R R_{i+1/2}^R \right] \quad (61)$$

$$Q_{i+1/2}^1 = \frac{b_{i+1/2}^+ + b_{i+1/2}^-}{b_{i+1/2}^+ - b_{i+1/2}^-} \alpha_{i+1/2}^1 - 2 \frac{b_{i+1/2}^+ b_{i+1/2}^-}{b_{i+1/2}^+ - b_{i+1/2}^-} \quad (62)$$

$$Q_{i+1/2}^2 = \frac{b_{i+1/2}^+ + b_{i+1/2}^-}{b_{i+1/2}^+ - b_{i+1/2}^-} \alpha_{i+1/2}^2 - 2(1 - \delta_{i+1/2}^2) \frac{b_{i+1/2}^+ b_{i+1/2}^-}{b_{i+1/2}^+ - b_{i+1/2}^-} \quad (63)$$

$$Q_{i+1/2}^3 = \frac{b_{i+1/2}^+ + b_{i+1/2}^-}{b_{i+1/2}^+ - b_{i+1/2}^-} \alpha_{i+1/2}^3 - 2(1 - \delta_{i+1/2}^3) \frac{b_{i+1/2}^+ b_{i+1/2}^-}{b_{i+1/2}^+ - b_{i+1/2}^-} \quad (64)$$

$$Q_{i+1/2}^4 = \frac{b_{i+1/2}^+ + b_{i+1/2}^-}{b_{i+1/2}^+ - b_{i+1/2}^-} \alpha_{i+1/2}^4 - 2 \frac{b_{i+1/2}^+ b_{i+1/2}^-}{b_{i+1/2}^+ - b_{i+1/2}^-} \quad (65)$$

mefvm implements this method a bit differently than explained here similar to the *Roe method*. It was quite hard to understand this implementation due to a lack of background knowledge and inconsistent notation schemes across different articles.

3.7 Rusanov [rusanov]

Nostalgia from homework 3 (Baygeldi-Kaya-Kakilli 2025), Rusanov uses "through" calculation schemes in Eulerian coordinates aiming to reduce the tangential discontinuities for 2-dimensional problems. (Rusanov 1962)

First Rusanov starts by defining the following:

$$\frac{\partial f}{\partial t} + \frac{\partial F^x}{\partial x} + \frac{\partial F^y}{\partial y} + \Psi = 0 \quad (66)$$

Where:

$$f = \begin{pmatrix} \rho \\ r \\ s \\ e \end{pmatrix}, F^x = \begin{pmatrix} r \\ p + ru \\ rv \\ (e + p)u \end{pmatrix}, F^y = \begin{pmatrix} s \\ su \\ p + sv \\ (e + p)v \end{pmatrix}, \Psi = \frac{\nu v}{y} \begin{pmatrix} \rho \\ r \\ s \\ e + p \end{pmatrix} \quad (67)$$

With $\nu = 0$ for plane flow, $\nu = 1$ if there is axial symmetry. Furthermore:

$$r = \rho u, \quad s = \rho v, \quad e = \frac{\rho(u^2 + v^2)}{2} + \frac{p}{k-1} \quad (68)$$

Rusanov then defines:

$$\phi = \begin{pmatrix} u \\ v \\ p \\ \rho \end{pmatrix}, \quad w = \sqrt{u^2 + v^2}, \quad c = \sqrt{\frac{kp}{\rho}} \quad (69)$$

With simple trigonometric expression for boundary interfaces. Rusanov then moves on to define the difference with $\Delta x = h_1$, $\Delta y = h_2$, and $\Delta t = r$. Furthermore, the value of any quantity, a , at a point with coordinates (mh_1, lh_2, nr) is denoted as $a_{m,l}^n$

$$h = \sqrt{h_1^2 + h_2^2}, \quad x_i = \frac{\tau}{h_i}, \quad x = \sqrt{x_1^2 + x_2^2} \quad (70)$$

Then Rusanov defines the following:

$$\begin{aligned} \Phi_{m+1/2,l}^x &= \alpha_{m+1/2,l}^n (f_{m+1,1} - f_{m,l})^n, \quad \alpha_{m+1/2,l}^n = \frac{1}{2}(\alpha_{m+1,l} + \alpha_{m,l})^n \\ \Phi_{m,l+1/2}^y &= \beta_{m,l+1/2}^n (f_{m+1,1} - f_{m,l})^n, \quad \beta_{m,l+1/2}^n = \frac{1}{2}(\beta_{m,l+1} + \beta_{m,l})^n \\ \alpha_{m,l}^n &= \omega x (w + c)_{m,l}^n \sin^2 X, \quad \beta_{m,l}^n = \omega x (w + c)_{m,l}^n \cos^2 X \end{aligned} \quad (71)$$

There are several stability conditions Rusanov states but suggests to use $\alpha_{m,l}^n = \beta_{m,l}^n = \frac{1}{2}$. After some further reductions, the numerical flux becomes (Rusanov 1962):

$$f_{m,0}^{n+1} = f_{m,0}^n - \tau \hat{\Psi}_{m,0}^n - \frac{x_1}{2} (F_{m+1,0}^x - F_{m-1,0}^x) - x_2 F_{m,1}^{yn} + \frac{1}{2} (\Phi_{m+1/2,0}^x - \Phi_{m-1/2,0}^x + 2\Phi_{m,1/2}^y) \quad (72)$$

$mef_v m$ utilizes a more concise code similar to the code written in Homework 3 (Baygeldi-Kaya-Kakilli 2025).

A table is shared below which compares all the advantages and disadvantages of the methods.

Method name	Advantages	Disadvantages
Roe [roe]	Accurate modeling of shocks and contact discontinuities. Suitable for high-speed flows and shock structures.	Instability in low-speed regimes. Risk of producing non-physical solutions.
RoeM [roem]	Stability in low-speed problems. More accurate results in low-speed regions (e.g., post-shock areas).	May not provide as sharp solutions as classic Roe in high-speed regimes.
Rotated-RoeM [rotated-roem]	Accurate resolution of oblique shocks and complex flow structures. Ideal for oblique flows in scramjet inlets.	Higher computational cost compared to Roe and RoeM.
AUSMPW+ [ausmpw+]	High resolution in shock and separation regions. High accuracy in aero-dynamic analyses.	High computational cost.
AUSM ⁺ -up [ausm+up]	Stable solutions at low Mach numbers. Accurate modeling of shock waves and separations.	Potential loss of accuracy in high-speed flows compared to other methods.
HLLEM [hllem]	Stable resolution of shocks and contact discontinuities. Provides more stability.	Diffusive tendency leading to loss of resolution.
Rusanov [rusanov]	Simple and fast method.	Low accuracy in shocks and contact discontinuities.

Table 1: Comparison of Numerical Flux Functions

Though not explained in detail in the previous section, a table was created comparing the different time discretization schemes:

LU-SGS	TVD-RK3
Efficient for steady-state solutions in both subsonic and supersonic flows.	Suitable for transient solutions in both subsonic and supersonic flows.
Requires fewer iterations for steady-state convergence, making it ideal for subsonic and steady supersonic flows.	Provides high-order accuracy, especially useful for resolving transient phenomena in both regimes.
Handles stiff nonlinearity effectively, making it robust for supersonic shock interactions.	Excels in resolving sharp gradients and discontinuities, such as shocks in supersonic flows.
Computational cost is higher due to matrix operations but fewer time steps are required.	Computational cost per step is lower but requires more time steps due to stability constraints, especially in subsonic flows.
Well-suited for steady subsonic flows and steady supersonic shock-dominated problems.	Performs better for time-dependent subsonic and supersonic flows, such as unsteady shock oscillations.
Memory requirements are relatively low due to its iterative nature.	Higher memory requirements because of intermediate stages in each time step.
Less flexible for complex boundary conditions in subsonic flows.	More flexible for implementing complex boundary conditions, especially in subsonic regimes.

Table 2: Comparison of LU-SGS and TVD-RK3 Methods for Subsonic and Supersonic Flow Solutions (Yoon and Jameson 1988, Gottlieb and Shu 1998)

4 Explanation of the Benchmark Problems

4.1 Forward Facing Slope

In the figures and table below, the domain and boundary conditions to be used for forward-facing benchmark are shown. This benchmark includes a right-moving Mach 3 fluid entering a wind tunnel, which reduces its height due to a step opposing the direction of the fluid.

In this benchmark problem, before starting the meshing process, it is known that there will be a shock around the 3rd wall. Therefore, applying a finer mesh to the area around the 3rd wall is of great importance for the accuracy of the solution.

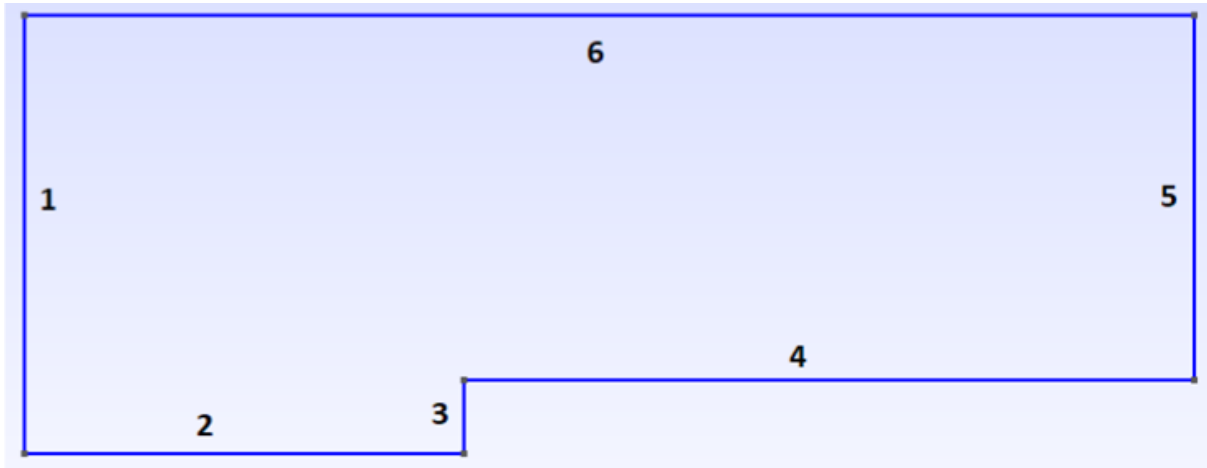


Figure 2: Forward facing step Benchmark Domain (M=3)

Face Number	Boundary Condition
1	Supersonic
2	Slip Wall
3	Slip Wall
4	Slip Wall
5	Subsonic Pressure Outflow
6	Slip Wall

Table 3: Boundary Conditions

The meshes produced for the Forward Facing Step benchmark are in the figures below.

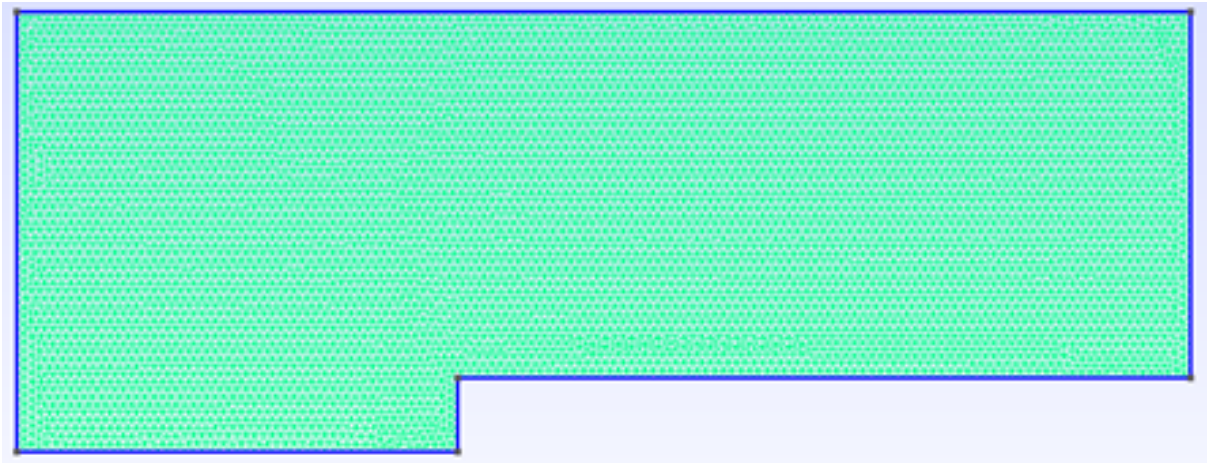


Figure 3: Forward facing step triangular

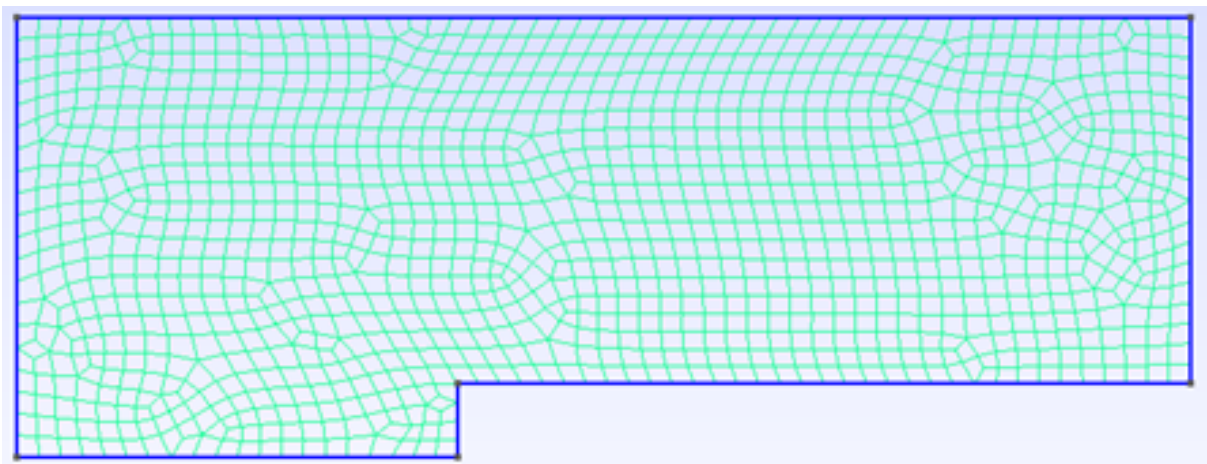


Figure 4: Forward facing step quadrilateral

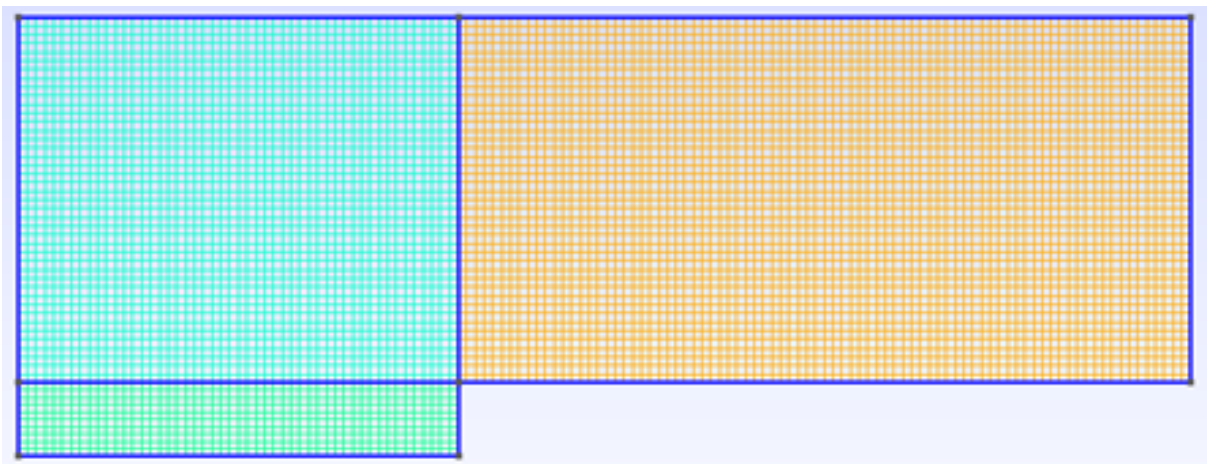


Figure 5: Forward facing step structural

Mesh name	Node Amount	Element Amount
Forward facing step triangular	7268	14540
Forward facing step quadrilateral	1249	1329
Forward facing step structural	6315	6600

Table 4: Mesh Properties of Forward-facing step benchmark

As can be seen from the table above, although the node numbers are very close to each other for “Forward facing step triangular” and “Forward facing step structural” there are almost twice as many elements in “Forward facing step triangular”. Furthermore, there are much fewer nodes and elements in the quadrilateral mesh than in the other two meshes. Therefore, it is expected that the analyses performed using “Forward facing step triangular” will be relatively more successful and accurate.

In the supersonic forward-facing step benchmark, flux functions must handle strong shocks, expansion waves, and complex flow features like shock-shock and shock-boundary layer interactions. AUSM⁺-up and AUSMPW+ are expected to yield the most accurate results due to their robust shock-capturing capability, low dissipation, and ability to resolve sharp flow features. Rotated-RoeM and RoeM also perform well, providing good resolution of oblique shocks and minimizing numerical artifacts in regions with strong gradients. The Roe solver is effective but may require entropy fixes to handle instabilities near shock interactions. HLLM offers robustness and stability but introduces excessive diffusion, which reduces the resolution of key flow structures. Rusanov is the least suitable, as its high dissipation smears shocks and fails to resolve intricate features accurately in such a challenging supersonic flow scenario.

4.2 Flow Over a Circular Bump

In the figures and table below, the domain and boundary conditions to be used for the flow over a circular bump benchmark are shown. This benchmark problem examines

transonic and supersonic flows over a bump within a channel geometry. For the transonic case, the circular bump on the lower wall has a thickness equal to 10% of its length, whereas, for the supersonic case, the arc-shaped bump's thickness is reduced to 4% of its length.

In this benchmark problem, before starting the meshing process, it is known that there will most likely be a shock on the circular bump in the supersonic case. Therefore, applying a finer mesh to the area above the circular bump is of great importance for the accuracy of the solution.

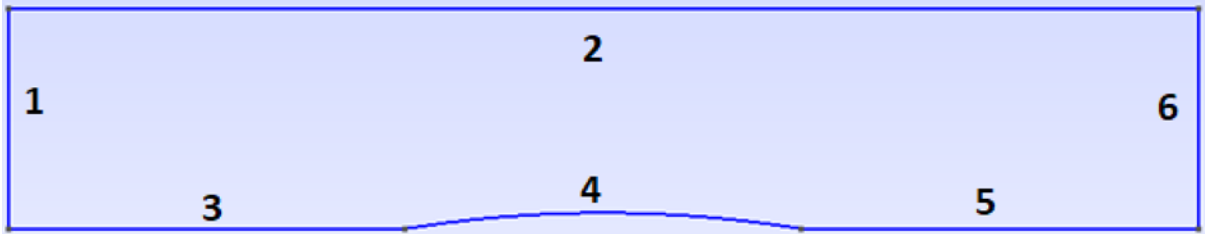


Figure 6: Supersonic Flow over a Circular Bump Domain $M_1=1.4$

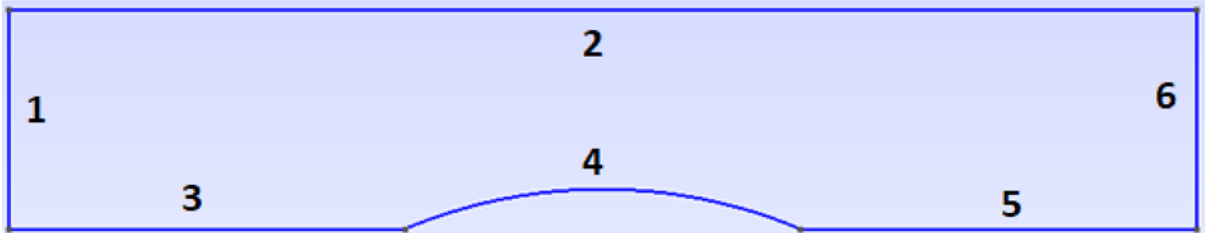


Figure 7: Transonic Flow over a Circular Bump Domain $M_1=0.675$

Face Number	Boundary Condition
1	Supersonic/Transonic Inlet
2	Slip Wall
3	Slip Wall
4	Slip Wall
5	Slip Wall
6	Subsonic Pressure Outflow

Table 5: Boundary Conditions

The meshes produced for the supersonic case are shown in the figures below.

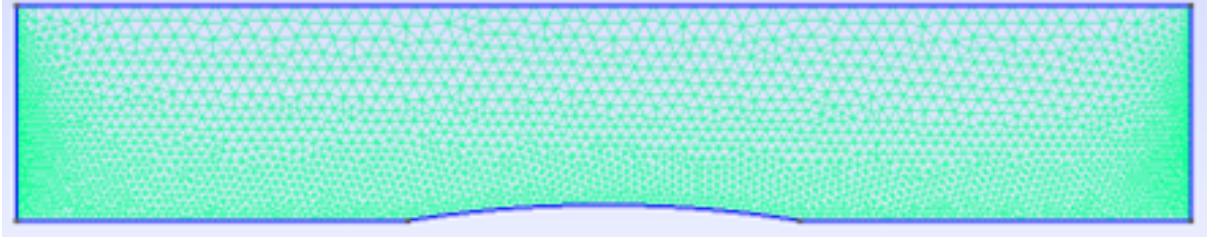


Figure 8: Supersonic flow over a circular bump mesh 1

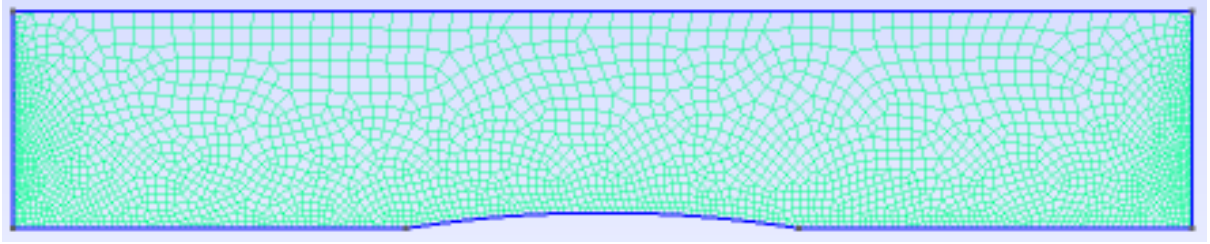


Figure 9: Supersonic flow over a circular bump mesh 2

As can be seen in the figures above, the circular bump is more finely meshed than the rest of the domain in both meshes. The purpose of choosing these two mesh types in this benchmark test is to determine the effect of triangular and quadrilateral mesh geometries on the obtained residual values.

Mesh name	Node Amount	Element Amount
Supersonic flow over a circular bump mesh 1	3167	6337
Supersonic flow over a circular bump mesh 2	3090	3274

Table 6: Mesh Properties of Transonic Flow Over a Circular Bump Benchmark

As can be seen from the table above, although the node numbers are very close to each other, there are almost twice as many elements in "Transonic flow over a circular bump mesh 1". Therefore, it is expected that the analyses made using "Transonic flow over a circular bump mesh 1" will be relatively more successful and accurate.

In the transonic flow over a circular bump benchmark, the performance of flux functions is determined by their ability to handle mixed subsonic and supersonic regions, including shock-boundary layer interactions. AUSM⁺-up and AUSMPW+ are expected to perform best, offering an accurate resolution of shocks and smooth transitions between flow regimes. RoeM and Rotated-RoeM are also strong contenders, effectively capturing shocks and mitigating instabilities near sonic points. The Roe solver provides reasonable results but may require entropy fixes to avoid nonphysical solutions in sonic regions. HLLM delivers robust but slightly diffusive solutions, resulting in less precise shock resolution. Rusanov performs poorly due to its high dissipation, which smears shocks and smooths critical flow features, making it unsuitable for high-resolution transonic benchmarks.

The meshes produced for the transonic case are shown in the figures below.

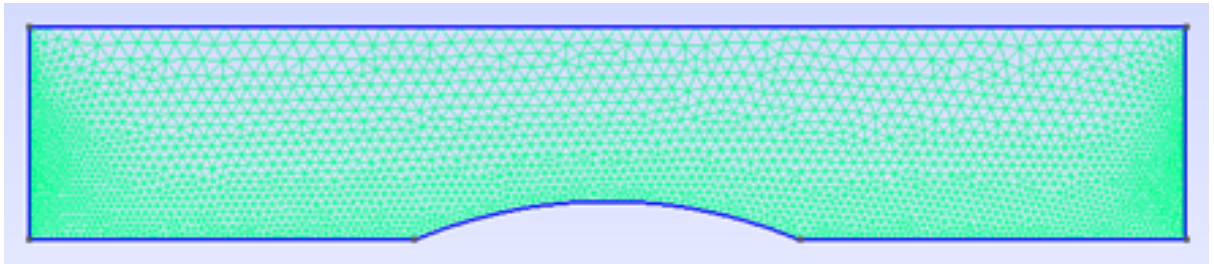


Figure 10: Transonic Flow Over a Circular Bump Mesh 1

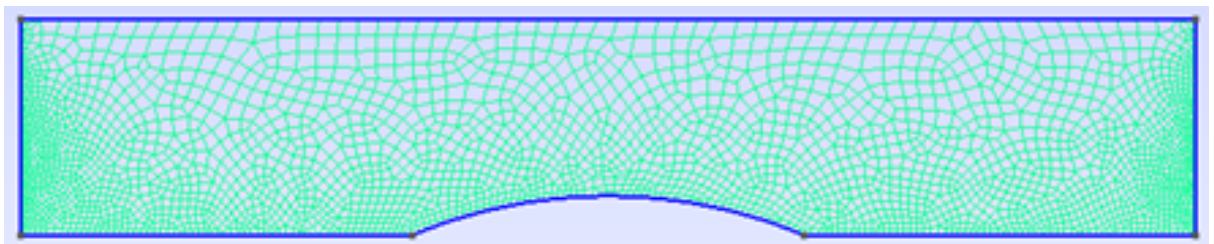


Figure 11: Transonic Flow Over a Circular Bump Mesh 2

As can be seen in the figures above, the circular bump is more finely meshed than the rest of the domain in both meshes. The purpose of choosing these two mesh types in this benchmark test is to determine the effect of triangular and quadrilateral mesh geometries

on the obtained residual values.

Mesh name	Node Amount	Element Amount
Transonic flow over a circular bump mesh 1	3173	6349
Transonic flow over a circular bump mesh 2	3102	3286

Table 7: Mesh Properties of Transonic Flow Over a Circular Bump Benchmark

As can be seen from the table above, although the node numbers are very close to each other, there are almost twice as many elements in "Transonic flow over a circular bump mesh 1". Therefore, it is expected that the analyses made using "Transonic flow over a circular bump mesh 1" will be relatively more successful and accurate.

In the transonic flow over a circular bump benchmark, the performance of flux functions is determined by their ability to handle mixed subsonic and supersonic regions, including shock-boundary layer interactions. AUSM⁺-up and AUSMPW+ are expected to perform best, offering an accurate resolution of shocks and smooth transitions between flow regimes. RoeM and Rotated-RoeM are also strong contenders, effectively capturing shocks and mitigating instabilities near sonic points. The Roe solver provides reasonable results but may require entropy fixes to avoid nonphysical solutions in sonic regions. HLLM delivers robust but slightly diffusive solutions, resulting in less precise shock resolution. Rusanov performs poorly due to its high dissipation, which smears shocks and smooths critical flow features, making it unsuitable for high-resolution transonic benchmarks.

4.3 Scramjet Inlet Flow Model with Different Boundary Conditions

The geometry, domain, and boundary conditions for the scramjet inlet flow model benchmark are given in the figure below. In this benchmark, a flow flowing at Mach 3 is simulated encountering an obstacle while passing through a converging channel.

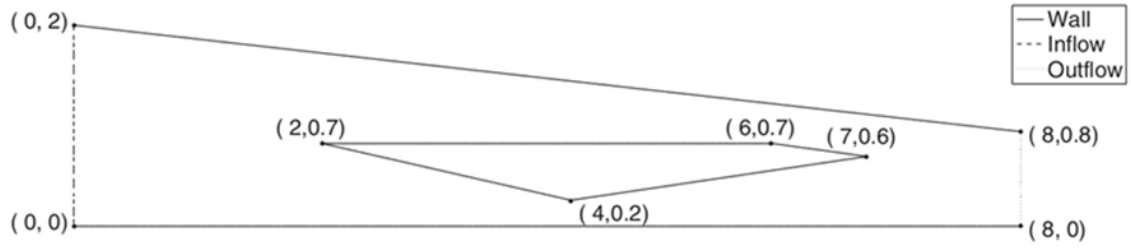


Figure 12: Sketch of the domain and the boundary conditions used in scramjet inlet model case

Before starting the mesh creation process, it is necessary to note that in a supersonic flow, any obstacle is very likely to create shock in the region where the obstacle is located. Therefore, a finer mesh should be created in order to get better results in the areas expected to be shocked. The meshes applied in this regard are shown in the figures below.

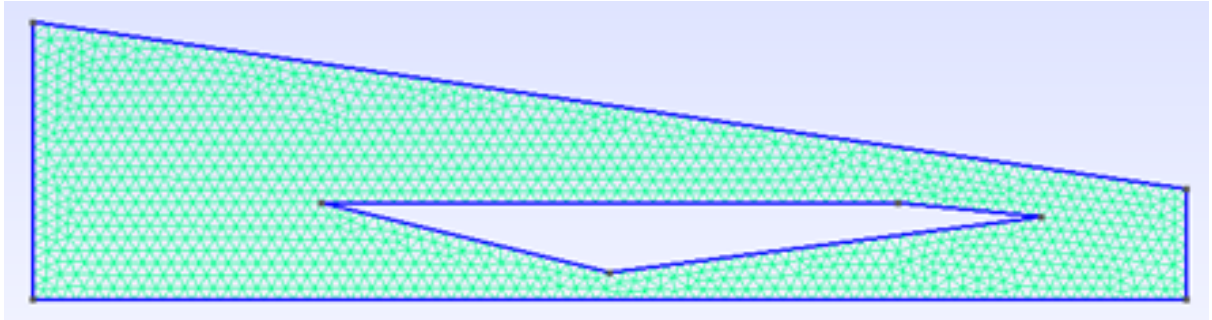


Figure 13: Scramjet inlet flow model mesh 1

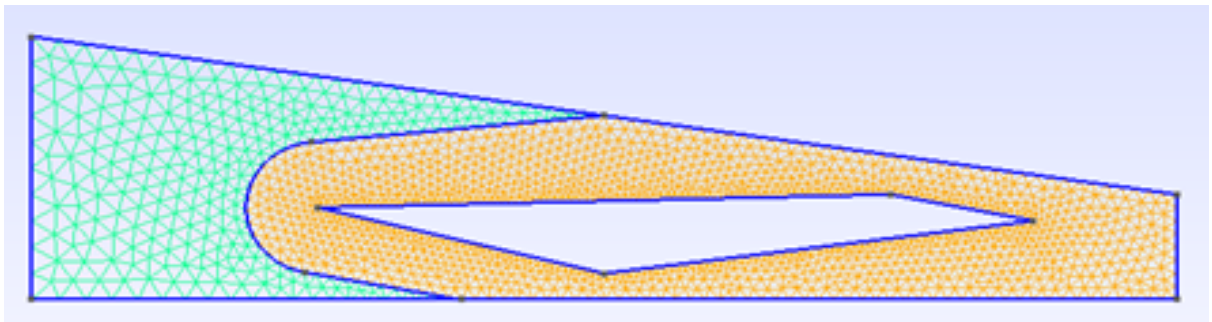


Figure 14: Scramjet inlet flow model mesh 2

In both Figure 2 and Figure 3, the boundary conditions are assigned as shown in

Figure 1, and the geometric dimensions are exactly the same. In the mesh shown in Figure 2, the entire domain is meshed with triangular mesh elements, with a finer mesh applied only to areas very close to the obstacle. The other mesh in Figure 3 is again composed entirely of triangular meshes, but a finer mesh is applied to include the entire surrounding of the obstacle.

Mesh name	Node Amount	Element Amount
Scramjet inlet flow model mesh 1	1341	2690
Scramjet inlet flow model mesh 2	1789	3638

Table 8: Mesh Properties of Scramjet inlet flow model benchmark

Considering the discarded meshes and the nature of the problem, the residual values obtained in "Scramjet inlet flow model mesh 2" are generally expected to be lower than the residual values obtained in "Scramjet inlet flow model mesh 1". The main reason for this is that while only the sharp changes caused by shock in the regions very close to the obstacle can be detected in "Scramjet inlet flow model mesh 1", on the other hand, all sharp changes caused by sock formed around the obstacle can be detected in "Scramjet inlet flow model mesh 2". This allows us to expect the residuals obtained in "Scramjet inlet flow model mesh 2" to be lower.

In this benchmark problem, all computations are done on the residual of the density, and some of the flux functions mentioned above are expected to yield better results than others. For density residual calculations, AUSM⁺-up and Rotated-RoeM are expected to yield the best results due to their superior shock resolution, low dissipation, and robustness in handling compressible flows. AUSMPW⁺ is also a strong choice, particularly in scenarios with complex shock and expansion wave interactions. The standard Roe solver and RoeM perform well but may require adjustments to mitigate instabilities. HLLM and Rusanov, while robust, are less favorable for achieving accurate density residuals in such applications.

5 Tests and Results

In this section of the report, relative tests of numerical flux functions and their results will be shared and discussed.

As an early warning, the initial condition and the outflow pressure are constant among the tested meshes and benchmark problems. The residual ρ for every test case can be found in the tables below.

Method Name	Triangular		Quadrilateral		Structured	
	lu-sgs	tvb-rk3	lu-sgs	tvb-rk3	lu-sgs	tvb-rk3
roe	0.09712	0.07654	0.01615	0.02866	0.10387	0.15758
roem	0.02318	0.02031	0.00776	0.01219	0.07344	0.08949
rotated-roem	0.00604	0.00529	0.03302	0.01605	0.03912	0.04148
ausmpw+	0.01251	0.01244	0.04079	0.05024	0.08107	0.08308
ausm+up	0.25721	0.38676	0.09322	0.12029	0.06009	0.08723
hllem	0.05009	0.06961	0.04653	0.03131	0.11251	0.14553
rusanov	0.00350	0.00988	0.01404	0.01206	0.02524	0.03009

Table 9: Results for Forward Facing Step Triangular & Quadrilateral & Structured

Method Name	Mesh 1		Mesh 2	
	lu-sgs	tvb-rk3	lu-sgs	tvb-rk3
roe	0.00285	0.00375	0.03130	0.03817
roem	0.00279	0.00394	0.00416	0.00652
rotated-roem	0.00010	0.00010	0.00973	0.01317
ausmpw+	0.00245	0.00284	0.01528	0.02141
ausm+up	0.00303	0.00429	0.03651	0.05332
hllem	0.00448	0.00465	0.02886	0.03445
rusanov	0.00298	0.00635	0.00267	0.00362

Table 10: Results for Supersonic flow over a circular bump mesh 1 & 2

Method Name	Mesh 1		Mesh 2	
	lu-sgs	tvb-rk3	lu-sgs	tvb-rk3
roe	0.00010	0.00010	0.01269	0.04222
roem	0.00087	0.00103	0.02406	0.04275
rotated-roem	0.00010	0.00010	0.0080	0.01440
ausmpw+	0.00516	0.00634	0.01146	0.01206
ausm+up	0.00597	0.00651	0.00931	0.02012
hllem	0.00010	0.00013	0.02095	0.03391
rusanov	0.00042	0.00089	0.00653	0.00674

Table 11: Results for Transonic flow over a circular bump mesh 1 & 2

Method Name	Mesh 1		Mesh 2	
	lu-sgs	tvb-rk3	lu-sgs	tvb-rk3
roe	0.04769	0.00375	0.04333	0.01543
roem	0.00051	0.00076	0.00074	0.00505
rotated-roem	0.00994	0.01041	0.00025	0.00354
ausmpw+	0.00785	0.03689	0.00298	0.00504
ausm+up	0.05614	0.07210	0.10301	0.10275
hllem	0.01647	0.00877	0.00075	0.00836
rusanov	0.00298	0.00635	0.00384	0.00133

Table 12: Results for Scramjet Inlet Flow Benchmark with Mesh 1 & 2

For the sake of simplicity of the commentary, all of the residuals will be plotted. In addition, the table shared below is a coding in which each method is paired with a number starting from one. The following figures are a comparison of all the residuals shared.

Corresponding Method	Encryption Number
roe	1
roem	2
rotated-roem	3
ausmpw+	4
ausm+up	5
hllem	6
rusanov	7

Table 13: Mesh Properties of Scramjet inlet flow model benchmark

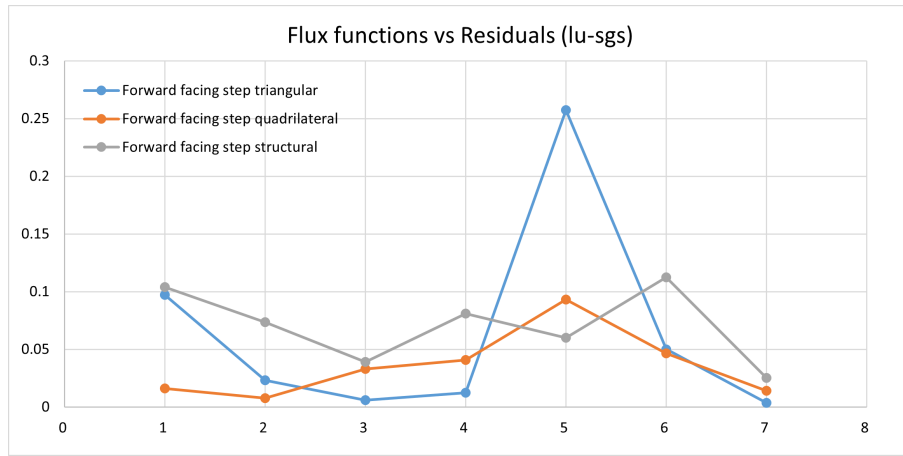


Figure 15: Forward Facing Step lu-sgs

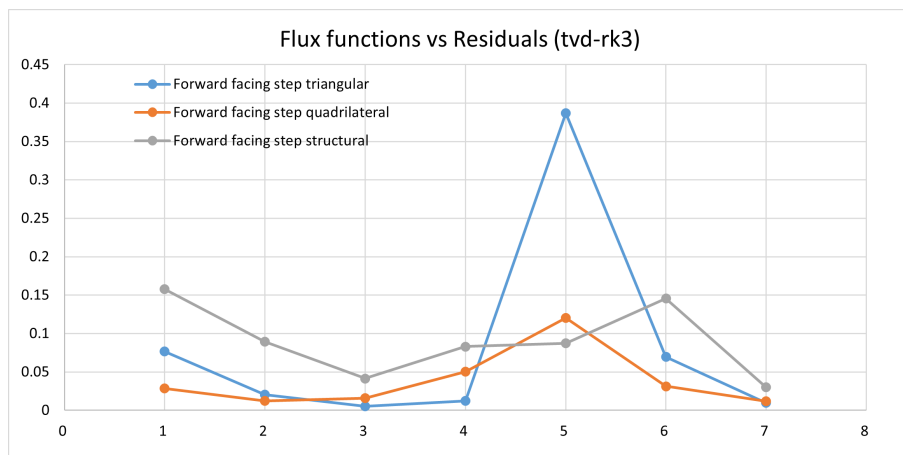


Figure 16: Forward Facing Step tvd-rk3

Starting with the first test case, the Forward Facing Step test case, as it can be seen clearly from Figures 13 and 14 the worst method for sharp bumps is AUSM⁺-up since it resulted in the biggest residual. However, this large residual is found when an unstructured mesh is used. For the structured case, the aforementioned method and test geometry resulted in a somewhat lower residual compared to the other methods.

An interesting observation is that although having the largest residual for one method, triangular mesh resulted in the lowest residuals for most of the methods tested except test cases 5 and 6. On the other hand, structured mesh geometry resulted in larger residuals for the most of test cases and the lowest for one test case which was AUSM⁺-up.

Test case 6, HLLEM, resulted in the lowest residual when an unstructured quadrilateral test mesh was used which makes it worth commenting on since most cases were dominated by triangular mesh geometries.

Comparing time discretization methods is not an easy task since there are no distinct trends present. However one can easily compare two methods by using the tables shared (Table 7-Table 10). For triangular mesh, tvd-rk3 has the lower residual until AUSM⁺-up. From this method and on lu-sgs is better. For quadrilateral test mesh the order changes. First lu-sgs has lower residuals until AUSM⁺-up then the other way around. For structured test case, lu-sgs has the lower residual for all cases.

Lastly comparing test methods is another subject to dive in. Back to the figures one can see a decreasing trend for triangular and structured until test method 3, Rotated-RoeM followed by an increase at method 4, AUSMPW+. Then their story diverges triangular one continues to rise while the structured one decreases. From here while the structured one increases, triangular one decreases. Lastly, they both decrease towards the method 8, Rusanov. Quadrilateral one increases up to case 5 and decreases from there.

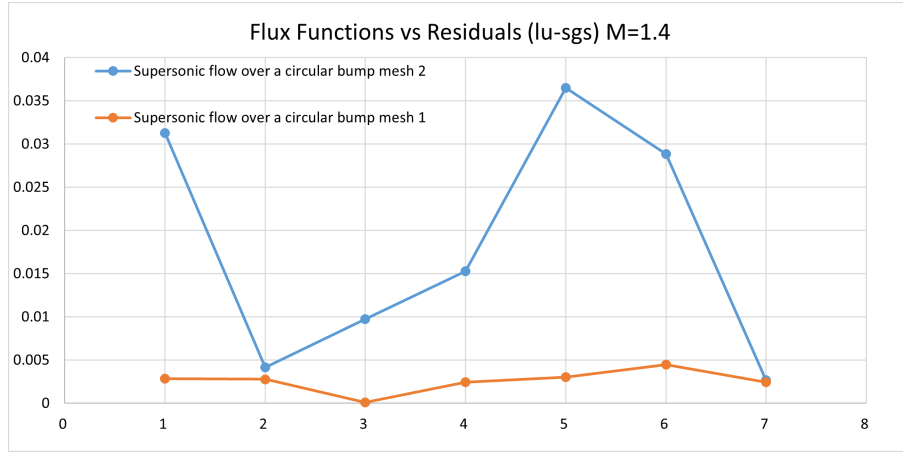


Figure 17: Supersonic Flow Over a Circular Bump lu-sgs

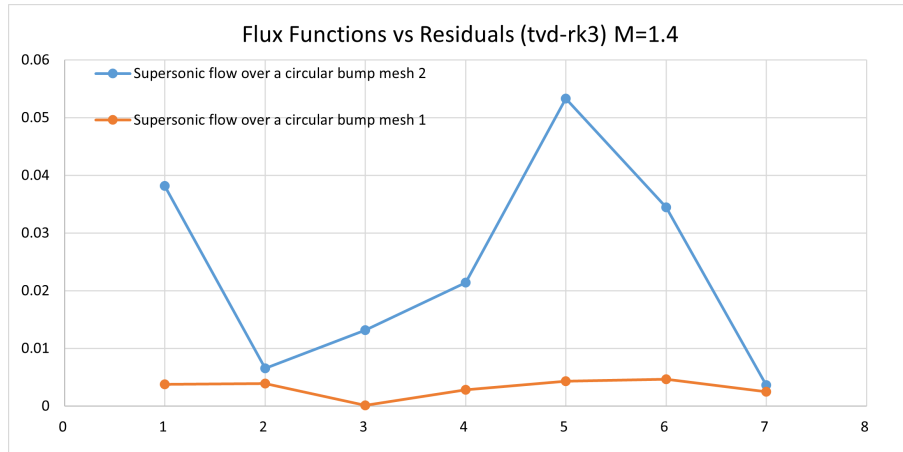


Figure 18: Supersonic Flow Over a Circular Bump tvd-rk3

Continuing with Supersonic Flow Over a Circular Bump, one can observe that the quadrilateral mesh type results in a lower residual for all seven methods and time discretization methods. Only in lu-sgs discretization with method 7, Rusanov it results in a lower residual.

A general rule can be the independence of quadrilateral mesh type with lu-sgs discretization. Although methods change, this mesh resulted in a near-constant, low residual despite the triangular one being much finer than the quadrilateral one. It would not be wrong to say that for a circular obstacle in a supersonic flow, the suitable mesh is the quadrilateral one. Triangular one first drops down rapidly, and increases until test case

5, AUSM⁺-up is reached. From 5 and on it decreases once again. This last comment is observed for both time discretization methods.

Another observation is that the lowest residual is reached when the Rusanov method is used for the triangular test case, on the other hand for the first time a solution is converged. When Rotated-RoeM is used for quadrilateral mesh type, the residuals sunk below the convergence criteria.

Also overall lu-sgs discretization resulted in lower residuals when compared to its counterpart.

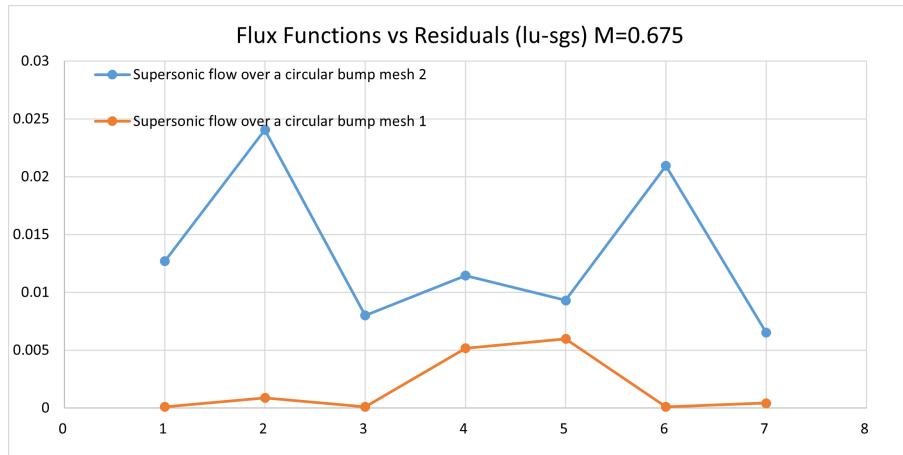


Figure 19: Transonic Flow Over a Circular Bump lu-sgs

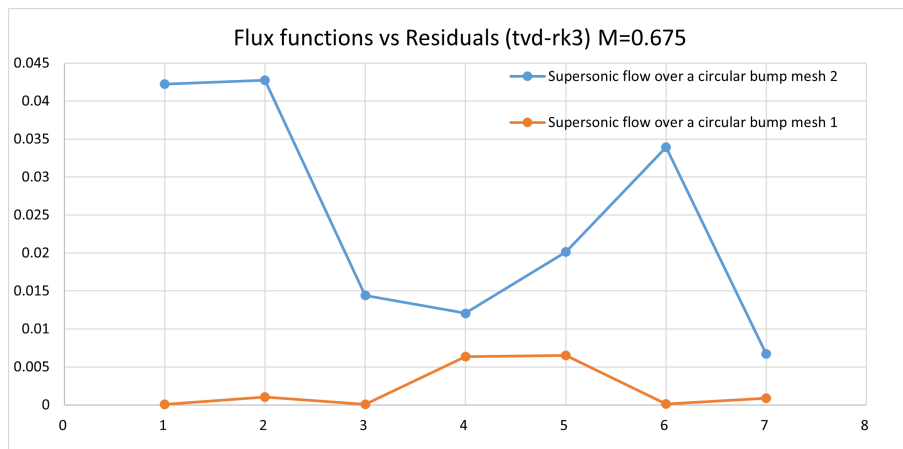


Figure 20: Transonic Flow Over a Circular Bump tvd-rk3

Moving on to the Transonic Flow over a Circular Bump, the results are nothing similar to the previous case. Residuals increase and decrease regularly in the triangular mesh type and it is relatively high when compared to quadrilateral mesh type. This quadrilateral mesh type also fluctuates but is not as aggressive as the triangular mesh type. Despite pushing the boundaries of flux methods, this particular test case has the highest convergence rate up until now. It converges for Roe and Rotated-RoeM in both time discretization methods and HLLEM for lu-sgs discretization.

For the triangular mesh type lowest residual is reached when Rotated-RoeM is used, this is true for the quadrilateral mesh type since it converges when that method is used.

Also, one little observation is that lu-sgs discretized triangular mesh resembles the ears of a cat.

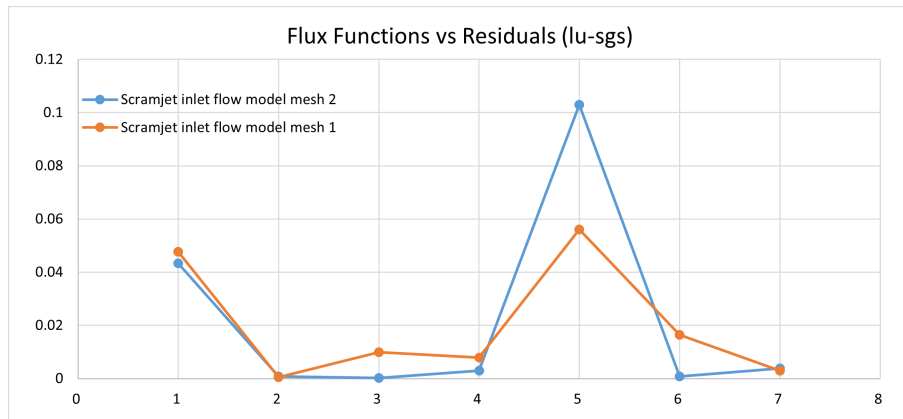


Figure 21: Scramjet Inlet Flow Model lu-sgs

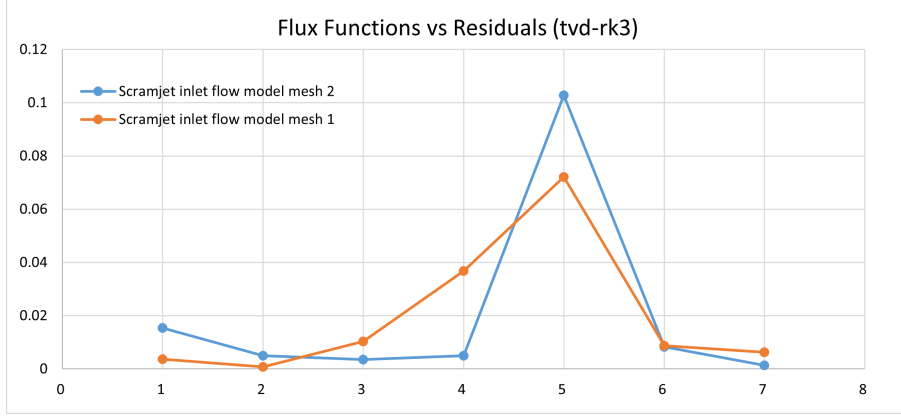


Figure 22: Scramjet Inlet Flow Model tvd-rk3

Lastly, an intriguing flow problem of the inlet of a scram jet is investigated. Taking a quick gaze at Figure 21, one can see that mesh structures follow a similar pattern. They both start with a relatively high residual which is followed by a sharp descent. Then they both increase moderately until method 5, AUSM⁺-up. When it reaches an abrupt jump happens then it is followed by a sharp decrease and another soft decrease follows the first one. About Figure 22 one can see that it has a similar trend with different initial conditions.

The discretization method of tvd-rk3 starts with surprisingly low residuals for both mesh types. While the mesh 2 has an increasing trend, the mesh1 counterpart decreases further. Overall mesh 1 has better results except when method 5, AUSM⁺-up in both and Rusonov in lu-sgs discretization is used.

The explicit method of discretization, tvd-rk3 resulted better only for the first two methods, the rest has a lower residual when tvd-rk3 method is used.

Comparison of the visualisation of these benchmarks with the literature is provided at the appendix

A Comparison With Literature

A.1 Forward Facing Step Benchmark

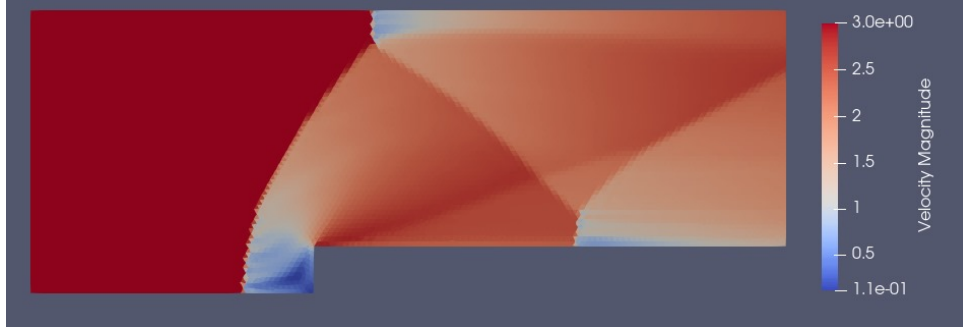


Figure 23: Visualization of the Forward Facing Step Benchmark (AUSMPW+ and lu-sgs)



Figure 24: Forward Facing Step Benchmark from Literature (Koellermeier and Samaey 2020)

As one can see, the visualization of the Forward Facing Step Benchmark obtained through *ParaView* shows similarity with the results of Koellermeier and Samaey 2020

A.2 Supersonic Flow Over Circular Bump Benchmark

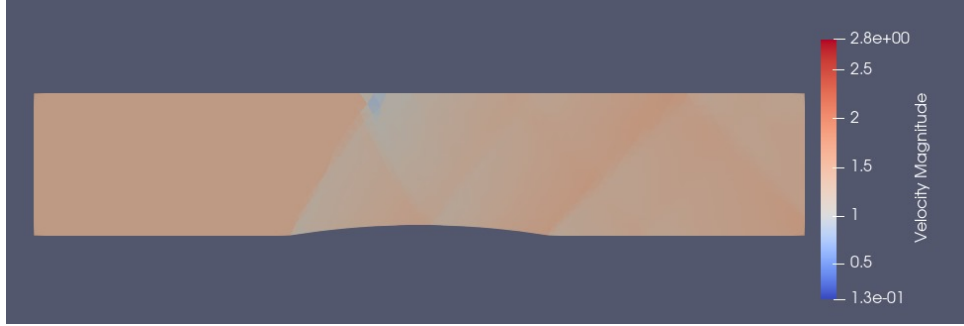


Figure 25: Visualization of the Supersonic Flow Over Circular Bump Benchmark (AUSMPW+ and lu-sgs)

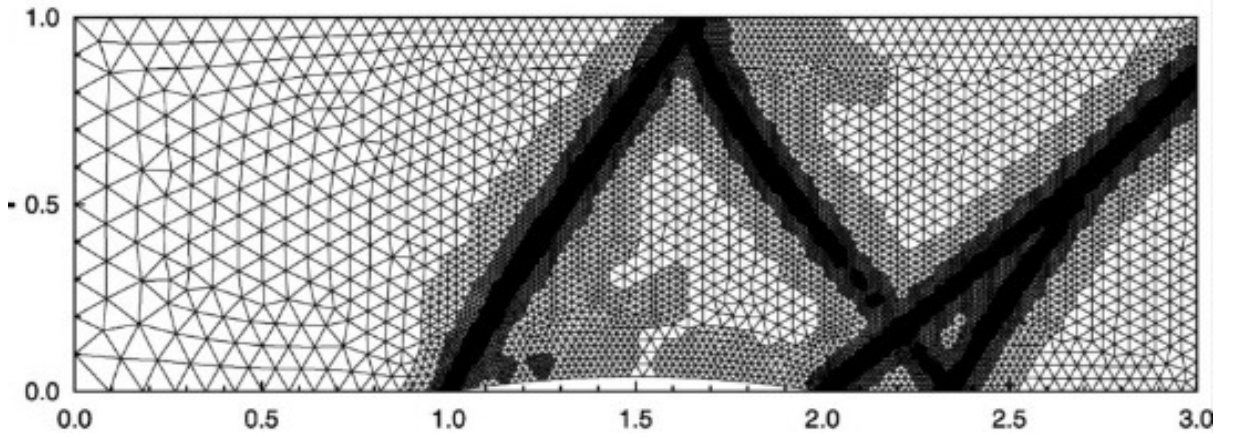


Figure 26: Supersonic Flow Over Circular Bump Benchmark from Literature (Ripley, Lien, and Yovanovich 2002)

Similarly, the obtained visualization shows similarity with the literature for the Supersonic Flow Over Circular Bump Benchmark (Ripley, Lien, and Yovanovich 2002)

A.3 Transonic Flow Over Circular Bump

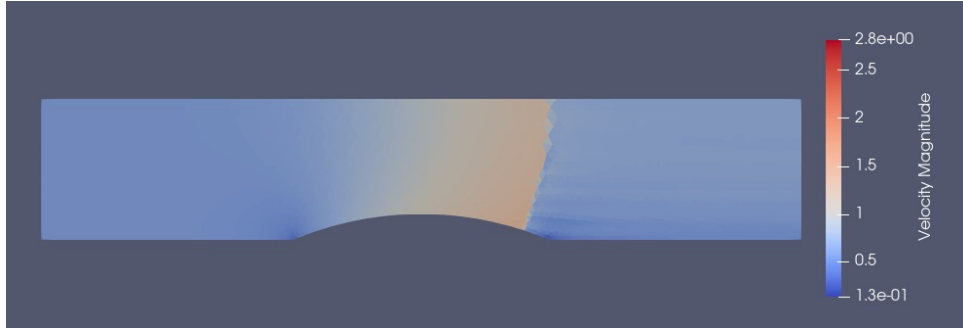


Figure 27: Visualization of the Transonic Flow Over Circular Bump Benchmark (AUSMPW+ and lu-sgs)

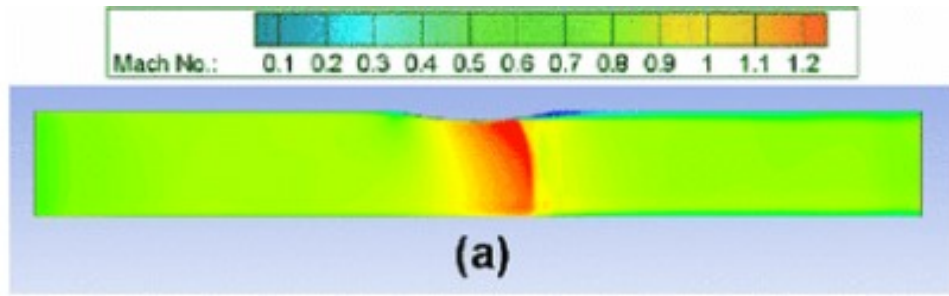


Figure 28: Transonic Flow Over Circular Bump Benchmark from Literature (Kuzmin 2016)

Unsurprisingly $me_{fv}m$ produces the desired result.

A.4 Scramjet Inlet Flow Model Benchmark

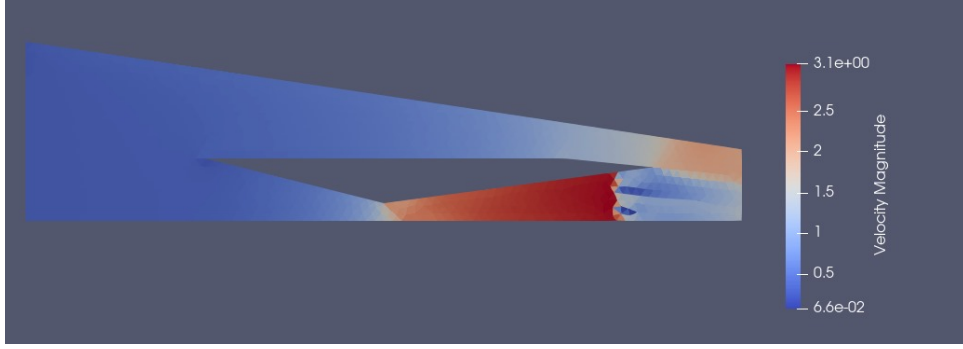


Figure 29: Visualization of the Scramjet Inlet Flow Model Benchmark (AUSMPW+ and lu-sgs)

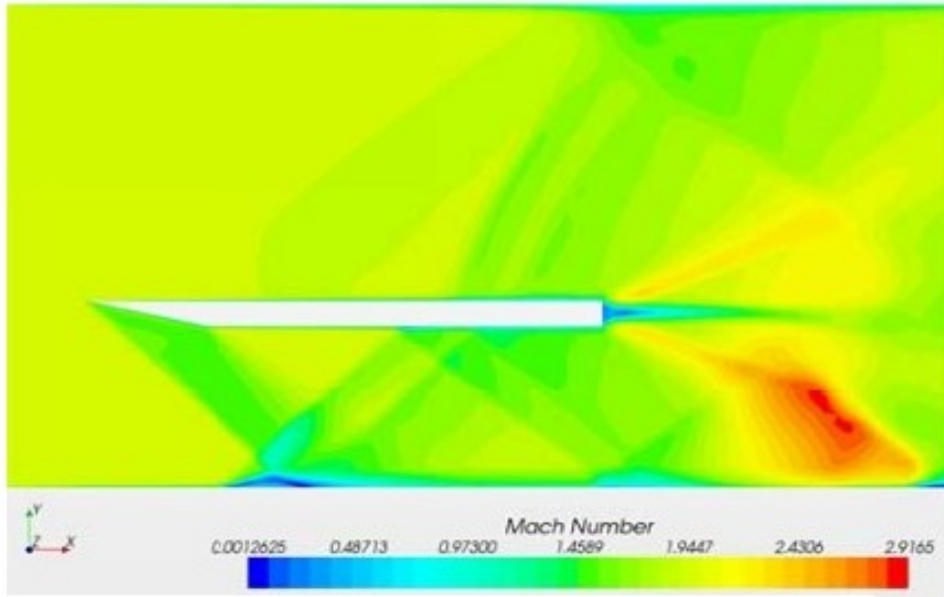


Figure 30: Scramjet Inlet Flow Model Benchmark from Literature (Seçkin and Yuçeil 2013)

As one can see, the figures are not similar. This is due to the fact that with the given case, a normal shockwave stands at the entrance of the model causing the actual Mach number of the inlet condition to be around 0.5. If the inlet Mach number is increased to 3.2 the following visualization is obtained with mem .

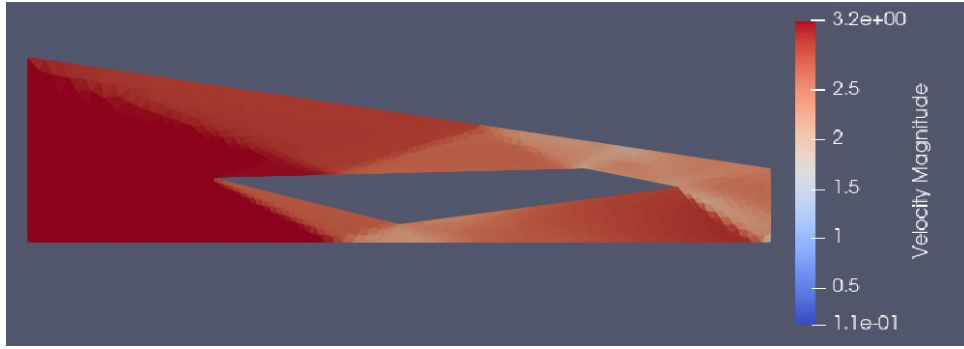


Figure 31: Visualization of the Scramjet Inlet Flow Model Benchmark Adjusted with $M = 3.2$ for Inlet Case (AUSMPW+ and lu-sgs)

The output shows a resemblance to the literature showing the oblique shock waves desirable in scramjet applications.

References

- Baygeldi-Kaya-Kakilli (2025). *Homework 2 Report*. Last accessed 20/01/2024. URL: https://github.com/uobaygeldi/ME485_HWs/blob/main/HW3%20Report.pdf.
- Choi, Seongyu et al. (2024). “Robust and accurate Roe-type Riemann solver with compact stencil: Rotated-RoeM scheme”. In: *Journal of Computational Physics* 505, p. 112913. ISSN: 0021-9991. DOI: <https://doi.org/10.1016/j.jcp.2024.112913>.
- Einfeldt, B et al. (1991). “On Godunov-type methods near low densities”. In: *Journal of Computational Physics* 92.2, pp. 273–295. ISSN: 0021-9991. DOI: [https://doi.org/10.1016/0021-9991\(91\)90211-3](https://doi.org/10.1016/0021-9991(91)90211-3).
- Elling, Volker (2009). “The carbuncle phenomenon is incurable”. In: *Acta Mathematica Scientia* 29.6, pp. 1647–1656. ISSN: 0252-9602. DOI: [https://doi.org/10.1016/S0252-9602\(10\)60007-0](https://doi.org/10.1016/S0252-9602(10)60007-0).
- Gottlieb, Sigal and Chi-Wang Shu (Jan. 1998). “Total variation diminishing Runge-Kutta schemes”. In: *Math. Comput.* 67.221, pp. 73–85. ISSN: 0025-5718. DOI: [10.1090/S0025-5718-98-00913-2](https://doi.org/10.1090/S0025-5718-98-00913-2).
- Karakuş, Ali (2024). *ME485 Lecture Notes*. Last accessed 20/01/2024. URL: <https://odtuclass2024f.metu.edu.tr/course/view.php?id=2835>.
- Kim, Kyu Hong, Chongam Kim, and Oh-Hyun Rho (2001). “Methods for the Accurate Computations of Hypersonic Flows I. AUSMPW+ Scheme”. In: *Journal of Computational Physics* 174, pp. 38–80. DOI: <https://doi.org/10.1006/jcph.2001.6873>.
- Kim, Sung-soo et al. (2003). “Cures for the shock instability: Development of a shock-stable Roe scheme”. In: *Journal of Computational Physics* 185.2, pp. 342–374. ISSN: 0021-9991. DOI: [https://doi.org/10.1016/S0021-9991\(02\)00037-2](https://doi.org/10.1016/S0021-9991(02)00037-2).
- Koellermeier, Julian and Giovanni Samaey (May 2020). *Projective Integration Schemes for Hyperbolic Moment Equations*. DOI: [10.48550/arXiv.2005.13914](https://arxiv.org/abs/10.48550/arXiv.2005.13914).
- Kuzmin, A. (May 2016). “Shock wave bifurcation in channels with a bend”. In: *Archive of Applied Mechanics* 86. DOI: [10.1007/s00419-015-1062-z](https://doi.org/10.1007/s00419-015-1062-z).

- Liou, Meng-Sing (2006). “A sequel to AUSM, Part II: AUSM+-up for all speeds”. In: *Journal of Computational Physics* 214.1, pp. 137–170. ISSN: 0021-9991. DOI: <https://doi.org/10.1016/j.jcp.2005.09.020>.
- Ripley, R.C., Fue-Sang Lien, and M. Yovanovich (July 2002). “Adaptive Mesh Refinement of Supersonic Channel Flows on Unstructured Meshes”. In: *International Journal of Computational Fluid Dynamics* 18, pp. 11–12. DOI: 10.1080/10618560310001634168.
- Roe, Philip (Oct. 1981). “Approximate Riemann Solvers, Parameter Vector, and Difference Schemes”. In: *Journal of Computational Physics* 43, pp. 357–372. DOI: 10.1016/0021-9991(81)90128-5.
- Rusanov, V.V. (1962). *Calculation of Interaction of Non-steady Shock Waves with Obstacles*. Technical translation. National Research Council of Canada. URL: <https://books.google.com.tr/books?id=9Tq5SgAACAAJ>.
- Seçkin, Serdar and Kemal Yuceil (Apr. 2013). “Flow Visualization of a Scramjet Inlet - Isolator Model in Supersonic Flow”. In: *EPJ Web of Conferences* 45, pp. 01099–. DOI: 10.1051/epjconf/20134501099.
- Yoon, Seokkwan and Antony Jameson (1988). “Lower-upper Symmetric-Gauss-Seidel method for the Euler and Navier-Stokes equations”. In: *AIAA Journal* 26.9, pp. 1025–1026. DOI: 10.2514/3.10007.